Poornima *et al.*
Journal of Engineering and Applied Science (2024) 71:151
https://doi.org/10.1186/s44147-024-00482-y

Journal of Engineering and Applied Science

RESEARCH Open Access

Corrosion behavior of combination of laser beam welded UNS S32304 + SS304L in 3.5% NaCl solution

Chodagam Lakshmi Poornima[1*], Chalamalasetti Srinivasa Rao[2] and Dantuluri Narendra Varma[3]

*Correspondence: poornima.chodagam@gmail.com

[1] Department of Mechanical Engineering, Sir C. R. Reddy College of Engineering, Vatluru, Eluru, Andhra Pradesh, India
[2] Department of Mechanical Engineering, Andhra University College of Engineering, Andhra University, Visakhapatnam, Andhra Pradesh, India
[3] Department of Mechanical Engineering, Andhra University, Visakhapatnam, Andhra Pradesh, India

Abstract

This study investigates the corrosion behavior of laser beam-welded UNS S32304 and SS304L in 3.5% NaCl solutions, focusing on the effects of temperature. The primary objective is to enhance the understanding of corrosion resistance in welded materials and inspire advancements in corrosion mitigation strategies. The methodology involves assessing corrosion resistance under varying temperatures and comparing the performance of laser beam welding (LBW) with that of the base metals. Scanning electron microscopy analysis reveals effective passivation, while quantitative analysis indicates differences in chloride ion coverage between the weld metal and base metals. Tafel plots and electrochemical impedance spectroscopy demonstrate enhanced corrosion potential and improved barrier properties for the weld metal. Results indicate a marginal reduction in corrosion resistance at 50 °C for both base metals. LBW metals corrosion resistance demonstrates superior performance, with only 5% reduction in breakdown potential compared to 10% in base metals. Compared to the base metal, it exhibits a substantial reduction in corrosion rate, ranging from 60 to 75%. This supports enhanced corrosion resistance and material stability. Additionally, similar results are observed after the analysis with scanning electron microscopy images, reinforcing the efficacy of LBW in improving corrosion resistance of LBW UNS S32304 and SS304L. These findings underscore the potential of LBW for applications requiring robust corrosion performance. By contributing to the understanding of the corrosion behavior of laser beam-welded materials, this study addresses a critical research gap in material science and corrosion engineering. Future research may explore long-term durability and corrosion resistance under diverse environmental conditions to further elucidate the mechanisms driving the observed differences in corrosion behavior.

Keywords: Corrosion behavior, Laser beam welding, UNS S32304, SS304L, Combination welding, 3.5% NaCl solution

Introduction

The corrosion of metals represents a significant challenge in the industrial sector and has been a subject of extensive investigation in recent years [1–3]. Most metal exhibit inherent instability and possess a natural inclination to react with the surroundings, forming chemical compounds in more stable states to achieve lower-energy levels. In

industrial environments, steel materials, especially mild steel, are frequently exposed and are highly susceptible to corrosion, particularly in aggressive media [4, 5]. Mild steel is commonly employed in various structural shape, such as beam, plate, bars, and pipe used in environments like saline water, which contain chloride known to be detrimental to steel [6]. Pitting corrosion, a common occurrence in stainless steels, occurs in the presence of chloride contains in the environments or when passivation is not fully completed. This type of corrosion is triggered by the breakdowns of the passive layers in stainless steels, influenced by metallurgical factor like inclusion, grains boundaries, or intermetallic constituent [7]. The disruption of the passive layers leads to the generation of electrochemical cells, with the active areas acting as the anode and the passive areas as the cathode. Metals and alloy that generates a thin protective film layer, typically 30 to 80 Å thick, known as the passive layer, are susceptible to this form of corrosion [8]. This implies that while the materials may undergo corrosion, the rate is negligible. However, when the protective films are breached, an electrochemical cell is formed, comprising of the anodes (a little exposed metallic areas due to film ruptures) and the cathode (the larger areas guarded by the film). The potential difference between these regions induces a high current flow, leading to fast corrosions of the anode areas. Once the initiation of pit formation occurs, it becomes an own-catalytic process, progressing independently. The composition of metals significantly impacts the LBW processes, which involve melting and joining metal component utilizing a high-powered laser beam. Combining materials with distinct properties, like UNS S32304 and SS304L stainless steel, in welding presents significant hurdles due to variations in thermal characteristics and material composition. These disparities often result in complications such as cracking and distortion during the welding process. Research [9] has demonstrated that proper selection of welding parameters can mitigate these challenges. Similarly, a study by [10] investigated the influence of process parameters on the properties of dissimilar material welds. Overall, successful welding of dissimilar materials relies on understanding the materials' properties and selecting appropriate welding parameters to achieve high-quality welds.

Duplex stainless steels (DSS) is a type of steel featuring two phasic microstructures comprising approximately 50% each of ferrite and austenite phases [11]. Among DSS, UNS S32304 is categorized as low alloy, offering cost advantages due to its minimum proportions of alloy element [12]. Another variant, 304L steel, falls into the middle alloy category, providing a broader range of applications, particularly notable for the inclusion of molybdenum in its composition. The distinctive feature of DSS lies in their combinations of maximum resistance to corrosion and robust mechanical strengths [13, 14]. Disruption of these passive layers exposes the steels to the risk of pitting corrosion. DSS are particularly susceptible to this form of corrosion when exposed to environments comprising chloride [15–18].

The resistance of stainless steel to pitting corrosions is enhanced by the presence of alloying element such as chromium, molybdenum, and nitrogen [19, 20]. When comparing DSS UNSS31803 and UNSS32304, a crucial distinction lies in the presence of molybdenum, with the former containing this alloying element. Various factors contribute to the generation of pits in stainless steels, including temperatures, factors of cleaning and surface finishes, microstructures, defect, environments, and applied potentials [21]. Pitting susceptibilities tend to rise with increasing temperatures, as evidenced by the

critical pitting temperatures (CPT), the minimum temperatures at which constant pits generation initiates. The presence of chloride in the environment can destabilize the passive layers and affects the steel's resistance to pitting corrosions. Additionally, the surface finish plays a significant role in pitting resistance. A more uniformly polished surface on the sample correlates with greater resistance to pitting.

While the study provides valuable insights into the corrosion behavior of laser beam-welded materials under varying temperatures, there are certain limitations and research gaps to consider. One drawback is the focus solely on a specific corrosive environment and temperature range, which may not fully represent all potential operating conditions. Additionally, while the superior performance of LBW is highlighted, further investigation into the long-term durability and corrosion resistance of the weld metal under diverse environmental conditions is warranted. Moreover, the quantitative analysis indicates lower Cl^- ion coverage on the weld metal compared to base metals, suggesting potential variations in corrosion mechanisms. However, the underlying factors driving these differences remain to be elucidated. Addressing these limitations and exploring the underlying mechanisms in more detail would enhance the comprehensiveness and applicability of the findings, providing a more robust understanding of the corrosion behavior of laser beam-welded materials.

Miranda-Pérez A. F. et al. [22] focused on gas metal arc welding's (GMAW) challenges in the hydrocarbon industry. The study simulated real petrochemical conditions, subjecting defect-free robotic GMAW samples to a 600-h corrosion test. Surprisingly, even corrosion-resistant DSS exhibited microstructural damage, highlighting the pivotal role of heat input in welding for optimal corrosion properties.

Torres C. et al. [23] investigated the impact of tungsten on the crevice corrosions resistances of super duplex stainless steel with varying tungsten content. Employing the PD-GS-PD techniques, the study determined critical crevices re-passivation temperatures at different tungsten levels. The findings revealed that the inclusion of tungsten, particularly in 2.1 wt.% W SDSS, significantly enhanced crevice corrosion resistance, indicating higher initiation and re-passivation crevice temperatures compared to W-free counterparts.

Singh J. et al. [24] delved into the application of autogenous electron beam welding (EBW) for producing full-penetration butt welds in 2205 DSS of varying thicknesses. The investigation comprehensively assessed metallurgical characteristics and corrosion behavior under different conditions.

Fedorov A. et al. [25] conducted an investigation into the impact of quench temperatures on the pitting corrosion resistances of least or lean DSS. Utilizing modeling of thermodynamics, they determined that same amounts of austenitic and ferritic are achieved at 1220 °C for the examining compositions. Experiment quenching from 1100 and 1200 °C revealed a significant increase in pitting potential with higher temperatures, attributed to the attainment of a favorable phase ratios.

Köhler M. L. et al. [26] investigated the potential of enhancing corrosion resistance and tensile strength in laser powder bed fusion (LPBF) processed alloys, focusing on an alternative to the widely used AISI 316L. Recognizing the limitations of LPBF for DSS due to the requirement for post-process annealing, the study aimed to identify a composition with improved properties without the need for such treatments.

Xiao Y. et al. [27] investigated the corrosion behaviors of 2205DSS in sulfides contains NaCl solution at various pH levels. Their study revealed that the addition of Na2S in 0.8 g/L NaCl solution improved pitting corrosions resistances in 2205 DSS. Notably, the pH played a pivotal role in influencing the corrosion mechanism, with the impact varying in 35 g/L NaCl solutions. At pH 11.5, Na2S enhanced pitting resistance, while at pH 9, 7, and 4, it promoted pitting corrosion.

Silva D. D. et al. [28] delved into the impact of sigma phases on the pitting corrosions behaviors of thermal-aged DSS. Employing structural, morphological, and electrochemical analyses, the study conducted potential dynamic tests in a 1-M NaCl solutions at different temperature. The innovative use of 3D roughness images, coupled with optical profilometry, proved effective in assessing surface degradation mechanisms resulting from pitting corrosion.

Oh S. et al. [29] delved into the corrosion behaviors of SDSS and its dependence on surface roughness. Recognizing the significance of practical corrosion resistance in SDSS, the study explored the impact on roughness of surface variations (110 to 1100 nm) on corrosion resistances and re-passivation, with and without pitting.

Rajaguru J. et al. [30] delved into the intricate interplay between machining-induced by integrity of surface and stress corrosion cracking (SCC) in SDSS. Recognizing the detrimental impact of poor machining characteristics on the surface integrity and subsequent tensile residual stress, the study investigated the formation of SCC under hostile chloride conditions.

Raj P. N. et al. [31] presented a comparative study on investigating the different properties, corrosions, and erosions-corrosions resistances of DSS, specifically the newly introduced ASTM A890 7A, against super duplex grades 5A and 6A.

Köse C. et al. [32] investigated the microstructure, hydroxyapatite (HA) formation, surface topography, and pitting corrosion properties of weld AISI 2205 DSS immersed in simulate body fluids (SBF) for varying durations. They found higher HA accumulation on the base material surfaces comparing to seam of the weld, with low crystallinity calcium-deficient carbonate HA observed on all surfaces.

Köse C. et al. [33] explored the impacts of weld heat treatments and welding heat on the surface characteristic, textures, microstructural feature, and mechanical behaviors of laser-weld sheets of AISI 904L super austenitic and AISI 317L austenitic stainless steels.

Köse C. et al. [34] explored inputs, and post weld heat treatments influence the surfaces, textures, microstructures, and mechanical characteristic of laser-welded AISI 2507 super duplex and AISI 317L austenitic stainless steel.

Köse C. et al. [35] investigated the weldability, microstructural characteristics, texture, and mechanical attributes of laser-welded connections between components of AM 316L and wrought sheets of 2507 super duplex stainless steel (W2507) and 904L super austenitic stainless steel (W904L). The investigation unveiled a refined microstructure featuring elevated dislocation density and varied texture patterns, alongside comparatively diminished mechanical properties in contrast to the base metals.

Ceyhun et al. [36] investigated the in vitro effect of CO_2 laser beam-welded AISI 2205 duplex stainless steel on the viability of L929 fibroblast cells, revealing higher cell viability in the welded sample compared to the base metal and control, suggesting suitability for biomedical applications.

The literature review provides valuable insights into various aspects of corrosion behavior, welding techniques, and material properties of stainless steels, particularly in challenging environments like petrochemical industries and biomedical applications. However, despite the extensive research in these areas, a significant research gap exists regarding the specific corrosion behavior of laser beam-welded combinations of UNS S32304 and SS304L stainless steels in 3.5% NaCl solutions. While studies have explored the corrosion resistance of individual stainless-steel grades and the effects of different welding techniques on their properties, there is limited research on the corrosion performance of welded combinations, especially under varying solution temperatures. Additionally, existing literature lacks comprehensive quantitative analysis of Cl^- ion adsorption and corrosion rates on both base metals and weld metal surfaces, as well as electrochemical behavior using techniques like Tafel plots and electrochemical impedance spectroscopy (EIS). Therefore, this study aims to bridge these gaps by systematically evaluating the corrosion resistance of laser beam-welded UNS S32304 and SS304L stainless steels, providing valuable insights into the effectiveness of the LBW process in enhancing corrosion resistance and material stability.

The experiment aims to investigate the corrosion behavior of an LBW combination of UNS S32304 and SS304L in a 3.5% NaCl solutions. The corrosion resistances of dissimilar metals welds are crucial for various industrial applications, and the interaction between DSS (UNS S32304) and austenitic stainless steel (SS304L) in a corrosive environment remains a complex area of study. Understanding the corrosion mechanisms and potential synergies or challenges in this welded combination is essential to ensure the integrity and durability of weld structures in marine and chloride-rich environments. This research addresses the need for comprehensive insights into the corrosion performances of dissimilar metal joint, contributing to the optimization of materials selection and welding processes for enhanced corrosion resistance.

Experimental setup

The experimental setup involved meticulous material preparation for the study, followed by precise weight loss measurements to assess corrosion behavior.

Electrochemical measurements are conducted to analyze the material electrochemical properties, complemented by scanning electron microscopy (SEM) for detailed surface characterization. Fig. 1 shows the laser welded specimens for corrosion test.

Materials preparation

LBW SS304L+UNS S32304, measuring 100 × 200 mm with a thickness of 3 mm and composed of Si (0.19%), P (0.42%), Mn (0.38%), C (0.14%), S (0.05%), and Fe (remainder), underwent weight loss and temperature effect investigations. Similarly, laser beam welded UNS S32304+SS304L sheets of the same composition, sized 0.5 cm^2, embedded in araldite and polished are used for electrochemical studies after degreasing with acetone. LBW joined dissimilar materials — SS304L and UNS S3204. All experiments utilized a corrosive solution of 3.5% NaCl (AR grade) prepared in distilled aqua solutions.

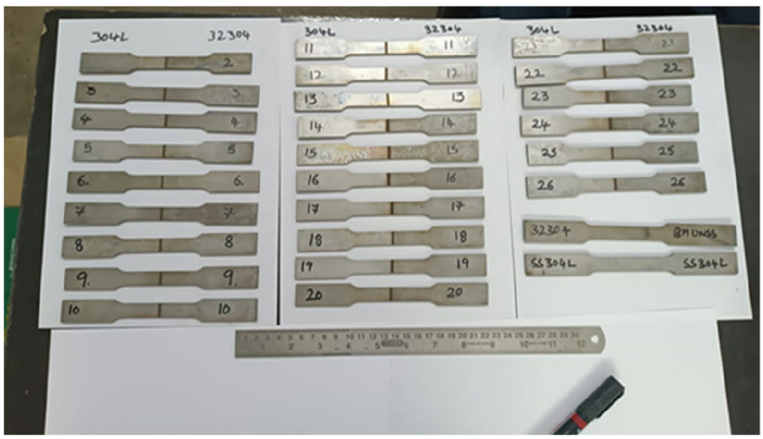

Fig. 1 Laser welded specimens for corrosion test

Measurement for weight loss

Measurements for weight loss are carried over a temperature range of 310 to 330 K within a thermostatic water bath, with each immersion lasting approximately 24 h. Utilizing a solution volume of 100 ml, LBW UNS S32304 + SS304L are extracted, meticulously cleansed with distilled waters, acetones, and air-dry before reweighing. The corrosion rates β and inhibition efficiencies (IE) are determined based on the recorded weight losses which are shown in Eq. (1).

$$\beta = \frac{N_b - N_a}{WT} \tag{1}$$

where N_b and N_a represent the initial and final weights of the specimen after dipping in the test solutions, respectively. W represents the surface areas of the specimens, and "T" signifies the duration of each single experiments. The calculation of inhibition efficiencies (IE%) value from weight losses (WL) data is performed using Eq. (2).

$$IE_{wc}(\%) = (\beta^o - \frac{\beta}{\beta^o}) \times 100 \tag{2}$$

where β^o represents the corrosion rate without inhibitor, while β signifies the corrosions rates in the existence of an inhibitors.

Electrochemical measurement

Electrochemical measurement assesses chemical systems by analyzing their electrical properties, including voltage, current, and impedance. Techniques such as potentiometry, voltammetry, and electrochemical impedance spectroscopy are used to study reaction kinetics, ion concentrations, and charge transfer processes. Widely applied across scientific disciplines, these methods are essential for developing materials, sensors, and medical diagnostic tools. Electrochemical measurement is conducted employing the H&CH Electrochemical Workstations Impedances Analyzers Model CHK 604E, equipped with I_R compensations capability, utilizing a tri-electrodes cells assembly. A bi-walls single-compartment cells, configured with mild steels as the working electrodes,

platinum electrodes as the counter electrodes, and calomel's as the base electrodes, is employed. Studies of polarization are executed with scan rates (ν/s) of 0.005, zero hold times at the equilibrium potential E_f, and a 2-s quiet time. AC impedance spectra are recorded using the same apparatus, measuring the true and imaginaries component of cell impedances in ohms across various frequencies. Equation (3) and Eq. (4) depict the charge transfer resistance R_{kt} and two-layer capacitances C_{el} values determined through specific relations.

$$R_{kt} = (R_m + R_{kt}) - R_m \tag{3}$$

$$C_{el} = \frac{1}{2}\Pi R_{kt} J_{max} \tag{4}$$

where C_{el} is the measure of corrosion damage, $J_{\max}$ represents the current density, and AC impedances are recorded with an initial potential set at 0, employing a high frequency of, low frequencies of 0.3 Hz, amplitudes of 0.008 V, and a quiet time of 2 s. The working electrode, with a surface area of 0.6 cm^2, underwent preparation involving abrasion with emery paper (grade 600–1200), rinsing with aqueous water, degreasing with acetones, and drying with cold air steam. Each experiment is iterated at minimum two times to ensure reproducibility. Inhibition efficiencies are determined using the formulas involving maximum frequency $J_{\max}$ and solution resistance R_m.

$$IE\% = \left(i^o_{corros} - \frac{i_{corros}}{i^o_{corros}}\right) \times 100 \tag{5}$$

where i^o_{corros} represents the current density of corrosions without an inhibitor and i_{corros} signifies the corrosions current density with the inhibitors which is shown in Eq. (5).

Scanning electron microscopy

SEM is a powerful imaging technique used to visualize the surface morphology and topography of materials at high resolution. It works by scanning a focused beam of electrons across the sample surface, generating signals such as secondary electrons, backscattered electrons, and X-rays, which are detected and used to create an image. SEM provides detailed information about the microstructure, composition, and texture of materials, making it invaluable in fields like materials science, nanotechnology, biology, and geology for characterizing samples at the micro- and nanoscale. LBW UNS S32304+SS304L are subjected to immersion in acid and chloride solutions both with and without the presence of an inhibitor for 24 h. Subsequently, after the designated periods, the specimen is removed and dried, and the surface film generated on the LBW UNS S32304+SS304L is analyzed using SEM (VEGA 3 TESCAN).

Laser beam welding (LBW) principle

LBW is a high-precision welding process that utilizes a concentrated laser beam as the heat source to join materials together. The laser beam is focused onto the workpiece, creating a localized heat source that melts and fuses the materials. LBW is characterized by its high-energy density, allowing for precise control over the welding process and the ability to weld highly reflective materials. This technique is commonly used in industries

such as automotive, aerospace, electronics, and medical devices, where precision, speed, and minimal heat-affected zones are critical. Employing the LBW techniques to join the recommended stainless steels introduces an innovative way to enhancing their structural performances. LBW offer an enhanced solution to addressing this issue and optimizing their combined benefit. The process involves focused on high-energy laser beam onto the area of joint, causing instant heating and normalized melting, resulting in a precise weld with minimal distortion and reduced impurities.

Fig. 2 illustrates the working principle of LBW, which typically comprises components such as a laser heads, feeding fibers, control units, assisted gas tanks, image processors, and powder deposition units. The laser head incorporates essential components like collimating unit, beam centering components, and nozzles for the amplifications and direction of the laser beam during joining of metal.

Welding procedure

The combination of UNS S32304 and SS304L is employed in fabricating weld specimens measuring 100 × 200 mm with a thickness of 3 mm, utilizing a laser seam welding system for joining. Table 1 displays the chemical composition and tensile characteristics of UNS S32304 and SS304L. Additionally, Table 2 presents the material properties

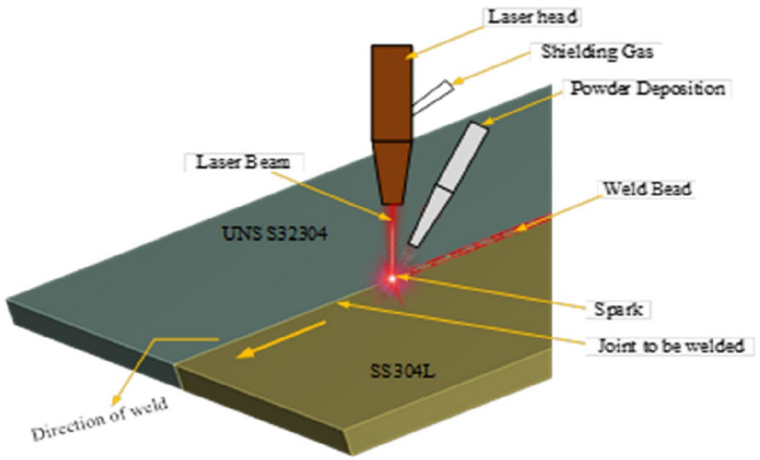

Fig. 2 Principle of LBW technique

Table 1 Materials composition

Chemical composition (%)	C	Mn	S	P	Si	Cr	Ni	N
UNS S32304	0.025	2.07	0.026	0.031	0.93	23	4.2	0.11
304L	0.028	1.96	0.023	0.035	0.96	19	10	-

Table 2 Material properties

Mechanical properties	Yield strength, MPa	Tensile strength, MPa	Elongation, %
UNS S32304	455	635	30
304L	320	560	49

Table 3 Input parameters of LBW

Input factor	Unit	Factor code	Low	Medium	High
Laser power	W	A	1200	1600	2000
Scanning speed	mm/min	B	2000	2500	3000
Beam diameter	µm	C	1	1.5	2
Focal position	mm	D	10	20	30

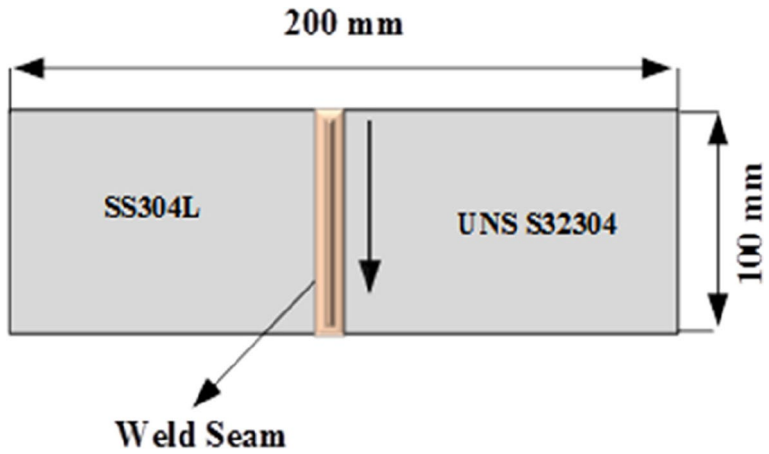

Fig. 3 Dimensions of the test specimen

specifically for LBW of UNS S32304 and SS304L. In the study, two scanning speeds are considered for two different cases, namely 1 mm/min and 2.5 mm/min.

Table 3 illustrates that laser power, measured in Watts (W), determines the energy emitted, affecting signal strength and range, with higher power being more potent yet potentially costly and hazardous. Scanning speed, in millimeters per minute (mm/min), dictates the pace of the laser beam across the target area, offering faster coverage at the expense of potential accuracy. Beam diameter, measured in micrometers (µm), influences data resolution, with a smaller diameter providing finer details but potentially making aiming challenging and being susceptible to scattering. Focal position, in millimeters (mm), influences the size of the laser spot on the target and energy delivery, impacting precision. Additionally, butt welding is employed in the fabrication process. Fig. 3 depicts the dimensions of the test specimen.

Procedure for preparation of samples for corrosion test

Corrosion resistance is crucial for the durability of welded stainless-steel combinations, especially in corrosive environments. This study focuses on evaluating the corrosion behavior of a laser beam-welded combination of UNS S32304 and SS304L in a 3.5% NaCl solution, emphasizing the impact of solution temperature. Meticulous sample preparation ensures standardized dimensions and surface conditions for accurate testing. Understanding the performance of the welded specimens under simulated corrosive conditions is vital for practical applications.

■ Cleaning of welded specimens: The welded specimens of UNS S32304 and SS304L, measuring 100 × 200 mm with a thickness of 3 mm, are thoroughly cleaned using a solvent wash and ultrasonic bath. This process ensures the removal of any surface contaminants or residues that could affect the accuracy of the corrosion test.

■ Surface preparation: Using precision tools, a rectangular area of 50 × 50 mm is marked on the surface of each specimen. This designated area is selected for corrosion testing. The surrounding regions are then masked off with high-quality adhesive tape to protect them from exposure to the corrosive solution.

■ Surface exposure: Within the marked zone, the surface of each specimen is carefully prepared to simulate real-world corrosion conditions. This involves roughening the surface using abrasive materials to create micro-scale defects that facilitate the initiation of corrosion.

■Preparation of corrosive solution: A 3.5% NaCl solution is meticulously prepared according to standardized protocols. The solution's concentration and pH levels are closely monitored to ensure uniformity and stability.

■ Immersion of specimens: The prepared welded specimens are securely mounted in corrosion test cells, with only the designated test area exposed to the corrosive solution. The specimens are positioned vertically in the test cells and immersed in the 3.5% NaCl solution for a predetermined period.

■Monitoring and evaluation: Throughout the corrosion test period, the specimens are regularly inspected for any signs of corrosion development. Visual assessments are conducted, and photographs are taken at regular intervals to document any changes in appearance or surface condition.

■ Conclusion of test: After the designated exposure period, the specimens are carefully removed from the corrosive solution. Any corrosion products or residues on the surface are gently cleaned off, and the specimens are allowed to air dry before further analysis.

In this study, hydrochloric acid (HCl) is employed as the acidic medium for corrosion testing. The preparation method involved diluting concentrated hydrochloric acid with distilled water to achieve the desired concentration, typically in the range suitable for corrosion testing. The exact concentration and pH of the acidic solution are carefully monitored and adjusted to ensure uniformity and stability throughout the testing process. By using hydrochloric acid as the corrosive medium, the study aimed to simulate real-world acidic environments and evaluate the behaviors of the LBW-SS combination under such conditions. This approach allowed for a systematic investigation into the material's resistance to corrosion in acidic media, providing valuable insights into its suitability for practical applications.

Preparation of corrosive medium

To prepare a corrosive medium with a 3.5% concentration of NaCl, a specific amount of NaCl needs to be accurately measured and dissolved in distilled or deionized water. For instance, to create a 100-ml solution, you would weigh 3.5 g of NaCl. The process involves carefully weighing the calculated amount of NaCl, adding it to a container, and gradually introducing distilled or deionized water while stirring continuously until

complete dissolution is achieved. It is crucial to ensure that no visible particles of salt remain, and the solution appears clear. Verification of the concentration is done through techniques like titration to confirm it aligns with the intended 3.5% NaCl concentration. This prepared corrosive medium is commonly utilized for corrosion testing of materials, providing a controlled environment that simulates real-world conditions. Safety precautions, including the use of personal protective equipment and working in well-ventilated areas, are essential throughout the process to maintain a secure working environment. Fig. 4a and b illustrates the configuration for preparing the corrosive medium.

Results and discussions

In the "Results and discussions" section, the corrosion outcomes of two distinct cases, Case 1 and Case 2, are discussed. This analysis includes parameters such as weight loss measurements, providing valuable insights into the corrosion behavior of the materials under consideration.

Corrosion test results

Corrosion test results are considered Case 1 and Case 2. The differentiation between cases is based on the welding parameters, which are taken into account for analysis.

Case 1: With laser power of 1.5 kW

In Case 1, a laser power of 1.5 kW is employed for welding dissimilar materials. The welding speed is 1 $mm/$ min, and the focal length is 150 mm. With these parameters, corrosion analysis is conducted after welding the materials.

Welding parameters for Case 1

Table 4 depicts the welding parameters for the first set of the corrosion test and which shows that the laser power is measuring 1.5 kW and denotes the energy delivered by the laser beam (LB), influencing weld depth and heat distortion. Welding speed, set at 1 $mm/$ min, determines the rate at which the LB traverses the workpiece, affecting both weld depth and duration. A beam diameter of 0.2 mm concentrates the LB, enabling the creation of narrower welds. The focal length, at 150 mm, plays a crucial role, influencing spot size and depth of penetration. The choice between argon or helium as an assist gas, coupled with a flow rate of 8 $L/$ min, shields the weld area from oxidation and contaminants. Beam quality, represented by a low M^2 value of 1.2, ensures a well-focused beam for consistent welds. A pulse frequency ranging from 5 to 10 Hz enables control over the speed of welds, with higher frequencies potentially introducing more heat distortion. The spot size, fluctuating between 0.3 and 0.5 mm, determines the width of the weld, and the 0.5 mm thickness of the material being welded impacts both penetration depth and welding speed. These parameters collectively contribute to the precision.

The corrosion analysis of the material reveals critical insights through various parameters. E_{corr} representing the corrosion potential indicates a balanced state at -0.0072 V, and metal oxidation and cathodic reduction reach equilibrium, suggesting minimal corrosion. However, I_{corro}, the corrosion current density, unveils a slow but consistent metal loss at $3.03x10^{-6}\,A/cm^2$.The counteracting force, R_p (polarization resistance), is robust

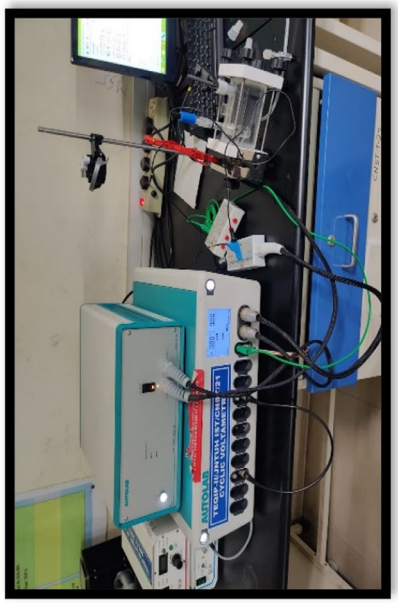

(b)

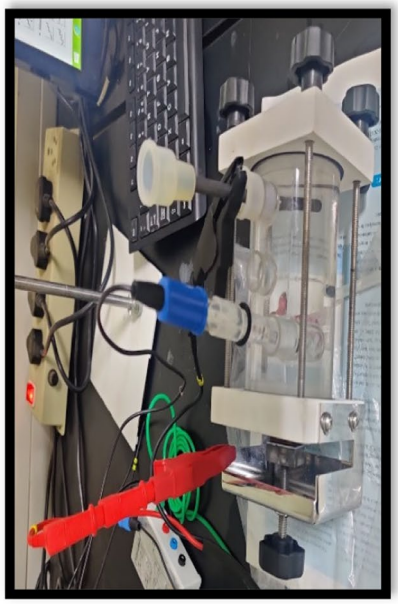

(a)

Fig. 4 **a** Electrode used in Tafel study. **b** Pitting corrosion setup

Table 4 Welding parameters for corrosion test 1

Parameter	Setting
Laser power	1.5 *kW*
Speed of welding	1 *mm*/ min
Beam diameter	0.2 mm
Focal length	150 mm
Assist gas	*Argon or Helium*
Gas flow rate	8 *L*/ min
Beam quality (M^2)	1.2
Pulse frequency	5–10 *Hz*
Spot size	0.3–0.5 mm
Thickness of material	0.5 mm

Table 5 Corrosion test result using Tafel data — Case 1

Corrosion parameters	Tafel data
Corrosion potentials $E_{corr}(V)$	−0.0072
Corrosion current density $I_{corro}(A)$	3.03×10^{-6}
Polarization resistance $R_p(Ohm)$	5034
Anodic Tafel slopes b_a (V/dec)	0.084
Cathodic Tafel slopes bc (V/dec)	0.061
Corrosion rates $C_{rate}(mm/y)$	0.03481

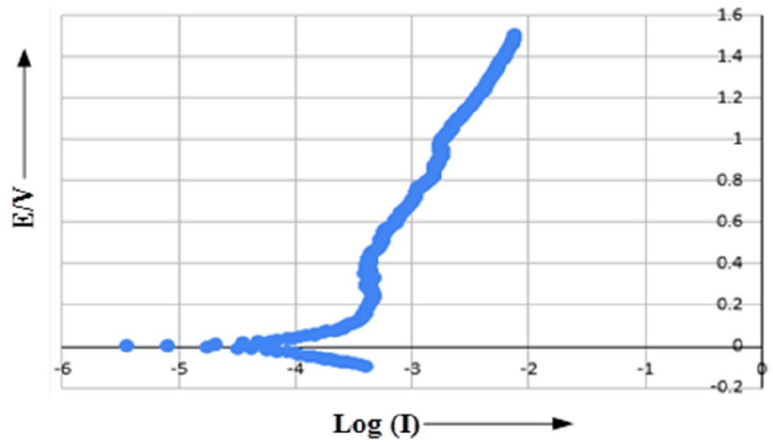

Fig. 5 Corrosion potential for Case 1

at 5034 Ω, highlighting the material's inherent defense against corrosion. Test result is shown in Table 5.

The Tafel slopes, b_a and b_c, elucidate specific mechanisms, with smaller values 0.084 V/dec for anodic and 0.061 V/dec for cathodic slopes suggesting surface chemistry limitations controlling corrosion rather than reactant diffusion which is shown in Fig. 5.

The comprehensive indicator, C_{rate}, estimates a low annual metal loss of 0.03481 mm/ year, showcasing the material's commendable corrosion resistance in the given environment. In essence, while the metal is not entirely immune, the amalgamation of a low

Table 6 Welding parameters for corrosion test 2

Parameter	Setting
Laser power	3 *kW*
Welding speed	2.5 *mm*/ min
Beam diameter	0.25 *mm*
Focal length	200 *mm*
Assist gas	*Nitrogen or Argon*
Gas flow rate	10 *L*/ min
Beam quality (M^2)	1.5
Pulse frequency	8–12 *Hz*
Spot size	0.4–0.6 *mm*
Thickness of material	4 *mm*

Table 7 Corrosion test results using Tafel data — Case 2

Corrosion parameters	Tafel data
Corrosion potential	− 0.0364
Corrosion current density	2.02×10^{-9}
Polarization resistance	2.02×10^{-9}
Anodic Tafel slopes	2.71×10^{6}
Cathodic Tafel slopes	0.033
Corrosion rates	0.02

corrosion potential, high resistance, and controlled reaction mechanisms collectively contributes to minimal metal loss, offering valuable insights for material selection and corrosion mitigation strategies to ensure prolonged performance.

Case 2: With laser power of 3 kW

In Case 2, a laser power of 3 kW is employed for welding dissimilar materials. The welding speed is 2.5 $mm/$ min, and the focal length is 200 mm. With these parameters, corrosion analysis is conducted after welding the materials.

Table 6 depicts the welding parameters for the second set of the corrosion test and which shows that the laser power is set to 3 kW and dictates the energy in the beam, allowing for the welding of thicker materials or faster speeds. Welding speed, set at 2.5 $mm/$ min, influences productivity and weld depth, with slower speeds resulting in deeper welds. Table 7 shows the corrosion test results using Tafel data — Case 2.

The beam diameter, set to 0.25, at the focal point impacts weld depth and control, with smaller diameters producing deeper welds but posing challenges in control. Focal length, set at 200, represents the distance between the lens and focal point, affecting beam size and intensity. Additional vital parameters include assist gas, gas flow rate, beam quality (M^2), pulse frequency, and spot size, all playing roles in controlling the welding process. These settings provide a starting point, and fine-tuning based on material, thickness, and desired weld quality is essential through experimentation. The weld metal exhibited a corrosion current density of 0.5 $\mu A/cm^2$ compared to 1.2 $\mu A/cm^2$ for

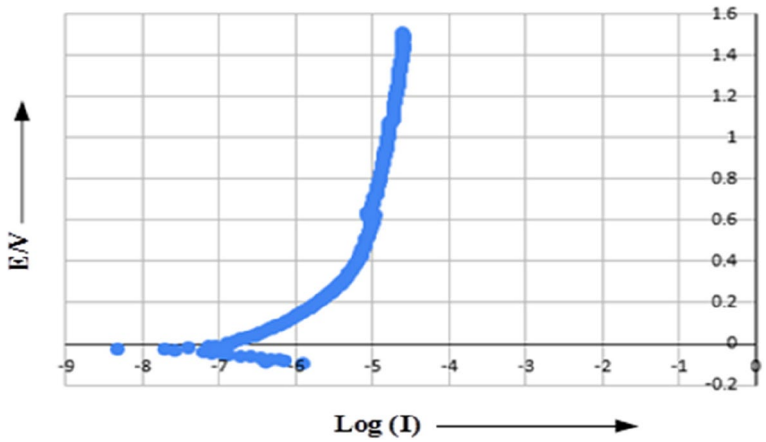

Fig. 6 Corrosion potential for Case 2

UNS S32304 and 2.0 $\mu A/cm^2$ for SS304L, signifying a 60% and 75% reduction in corrosion rate, respectively.

The corrosion characteristics of a metal are assessed through various electrochemical parameters. The corrosion potential E_{corr} in the image is measured at -0.0364, indicating the potential at which anodic and cathodic currents are equal, reflecting the metal's susceptibility to corrosion. The corrosion current density I_{corro}, quantified at 2.02×10^{-9}, signifies the rate at which metal ions dissolve into the electrolyte, representing the corrosion rate. Polarization resistance R_p, registered at 2.02×10^6, gauges the electrode's resistance to current flow, elucidating the ease of the corrosion reaction.

Tafel slopes (b_a and bc), crucial for determining corrosion mechanism, reveal in the image an anodic slope of $2.71 \times 10^6\ V/dec$ and a cathodic slope of $0.033\ V/dec$. Despite the relatively low corrosion rate of $0.02\ mm/y$, the high anodic Tafel slope suggests that enhancing conditions favoring the anodic reaction could escalate the corrosions rates. It is vital to acknowledge that these values are subject to material, environmental, and test condition variations, necessitating consultation with a corrosion expert for accurate interpretation of corrosion test results which is shown in Fig. 6.

Measurement of weight loss

Table 8 presents the computed corrosion rates and inhibition efficiencies for LBW UNS S32304+SS304L in a 3.5% NaCl environment, derived from weight loss measurements. The plots demonstrate a positive correlation between inhibition efficiency and the increasing concentration of NaCl.

Notably, Fig. 7 emphasizes that the inhibitory effect of LBW UNS S32304+SS304L on corrosion in chloride medium is concentration dependent, suggesting heightened efficiency at higher concentrations.

Electrochemical impedance spectroscopy

EIS is a powerful electrochemical technique used to characterize the electrical behavior of electrochemical systems, particularly in corrosion studies. It involves applying a small amplitude alternating current (AC) signal to the system and measuring the resulting

Table 8 Influence of temperatures of DSS in 3.5% NaCl at varied concentration

Temperatures (K)	Concentrations (M)	Corrosion rate ($\times 10^{-6}$)	Inhibition efficiencies (%)
310	Blank	5.6	-
	0.00002	2.8	50.84
	0.00004	3.4	49.89
	0.00006	2.1	56.56
	0.00008	1.9	61.00
	0.0001	1.6	67.66
315	Blank	4.7	-
	0.00002	2.9	37.66
	0.00004	2.6	46.66
	0.00006	2.3	53.18
	0.00008	2.1	57.53
	0.0001	1.8	64.05
320	Blank	4.72	-
	0.00002	3.01	36.18
	0.00004	2.76	42.53
	0.00006	2.43	48.94
	0.00008	2.21	53.20
	0.0001	1.93	59.58
325	Blank	4.92	-
	0.00002	3.21	34.70
	0.00004	2.83	40.86
	0.00006	2.58	46.96
	0.00008	2.38	51.03
	0.0001	2.18	55.12
330	Blank	5.01	-
	0.00002	3.36	31.96
	0.00004	3.06	37.96
	0.00006	2.81	44.02
	0.00008	2.56	48.01
	0.0001	2.26	54.03

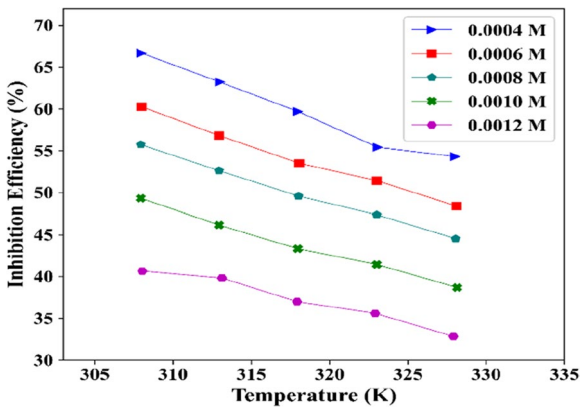

Fig. 7 Arrhenius plots for LBW UNS S32304 and SS304L

Table 9 Electrochemical impedance parameter for LBW UNS S32304 and SS304L 3.5% NaCl

$C_{inc}(M)$	$R_s(\Omega cm^2)$	$R_{kt}(\Omega cm^2)$	$C_{de}(F/cm^2)$	%I.E
-	13.17	158.83	2.306×10^{-5}	-
0.0004	12.28	234.54	1.569×10^{-5}	33.55
0.0006	11.93	252.25	8.205×10^{-6}	38.88
0.0008	13.62	257.81	7.303×10^{-6}	37.25
0.00010	11.88	342.32	6.790×10^{-6}	54.46
0.001 2	8.57	391.53	4.989×10^{-6}	58.06

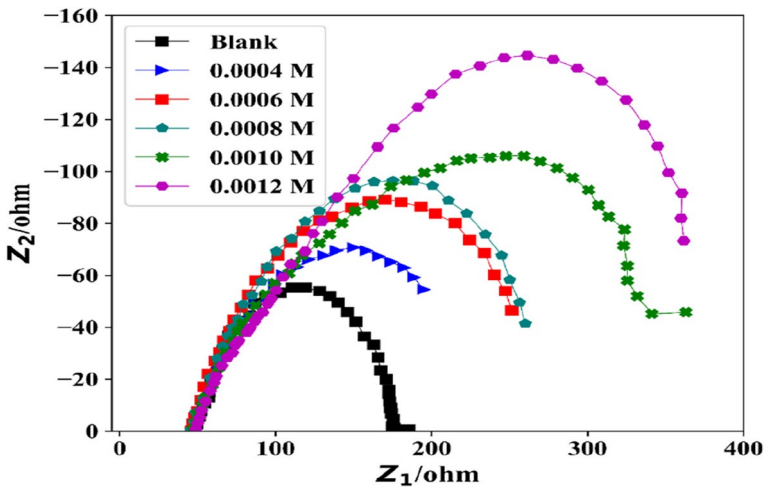

Fig. 8 Nyquist plots for LBW UNS S32304 and SS304L immersed in 3.5% NaCl

impedance response across a range of frequencies. EIS provides valuable information about the electrical properties of the system, including its resistance, capacitance, and charge transfer processes. By analyzing the impedance spectra obtained at different frequencies, researchers extract parameters such as polarization resistance, charge transfer resistance, and double-layer capacitance, which are indicative of the corrosion behavior and electrochemical kinetics occurring at the electrode surface. EIS is widely used in corrosion studies to assess the corrosion rate, evaluate the effectiveness of corrosion protection coatings, investigate corrosion mechanisms, and optimize corrosion inhibition strategies. It is a nondestructive and highly sensitive technique that offers insights into the fundamental electrochemical processes governing corrosion phenomena. Corrosion behavior of LBW UNS S32304 and SS304L in 3.5% NaCl mediums is studied by EIS measurement present in Table 9.

Fig. 8 shows the Nyquist plot of the impedances data as depress capacitive semicircle. The diameters found by the intercepts of each of these loops and the horizontal Z real axes are related to the charge transfers resistances. Hence, a maximum value indicates strong resistances against corrosions.

The inhibition efficiencies are measured from the relations given in Eq. (6):

Table 10 Potentiodynamic polarization parameters for the corrosion of LBW UNS S32304 + SS304L in 3.5% NaCl

$C_{inc}(M)$	$E_{corro}(mV)$	$i_{corro}\left(Acm^{-2}\right)$	C_b	b_a	P_r	$^o/d.E$
-	− 0.849	3.250×10^{-6}	11.84	8.324	851.0	-
0.0002	− 0.831	2.742×10^{-6}	11.54	6.211	1413.7	23.59
0.0004	− 0.763	1.567×10^{-6}	3.776	13.16	1547.0	31.37
0.0006	− 0.767	0.843×10^{-6}	6.210	13.75	2312.8	56.11
0.0008	− 0.834	0.789×10^{-6}	13.41	7.323	2714.0	63.49
0.001	− 0.815	0.689×10^{-6}	8.833	8.786	2418.2	65.94

$$I.E\,\% = (R_{kt}^1 - \frac{R_{kt}}{R_{kt}^1})\text{X}100 \tag{6}$$

where R_{kt}^1 and R_{kt} are the values of the charge transferring resistances observed of inhibitor molecules. The augmentation in charge transfer resistances attributed to the presence of the inhibitor arises from alterations in the chemical compositions of the surface films.

This transformation occurs primarily through the inclusion of inhibitor molecules into the films, especially at defect site characterized by low ionic resistances. The molecules integrated into the film generate high-resistance compounds.

The findings indicate that 3.5% of NaCl exhibits inhibitory effects on the corrosion of LBW UNS S32304 + SS304L in both acidic and chloride environments, with the primary corrosion control mechanism being charge transfer. The observed increase in R_{kt} values suggests improved corrosion resistance, highlighting the corrosion-inhibiting potentials of NaCl.

Potentiodynamic polarization studies

Potentiodynamic polarization studies are a fundamental electrochemical technique used to evaluate the corrosion behavior of metallic materials. This technique involves sweeping the electrode potential at a constant rate while measuring the resulting current response. By plotting the resulting polarization curve, which typically shows the current density (logarithmic scale) versus the electrode potential, researchers extract important electrochemical parameters such as corrosion potential (Ecorr) and corrosion current density (icorr). These parameters provide insights into the corrosion resistance of the material, its tendency to corrode, and the kinetics of the corrosion processes. Potentiodynamic polarization studies are commonly used to assess the effectiveness of corrosion protection methods, investigate the mechanisms of corrosion, and compare the corrosion resistance of different materials or surface treatments. They are valuable tools for understanding and controlling corrosion in various industrial and engineering applications. Table 10 displays the computed polarization parameters for 3.5% NaCl, while Fig. 9 illustrates the anodes and cathodes polarizations curve related to LBW UNS S32304+SS304L corrosion in a chloride environment. The inhibitions efficiency is calculated by the following expressions:

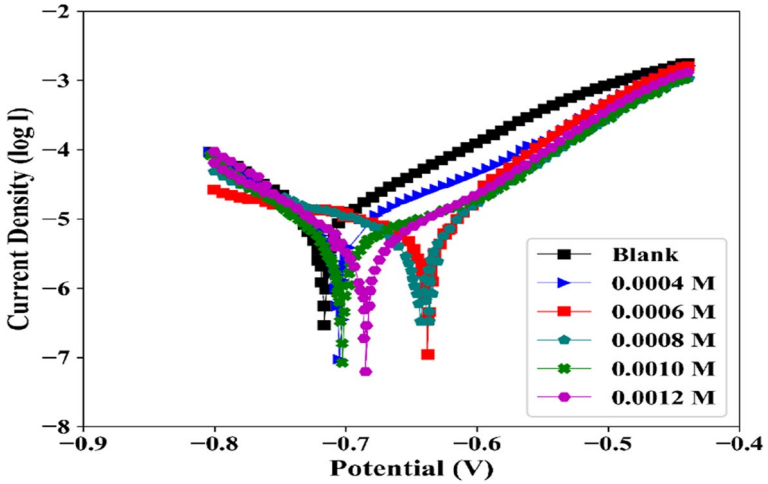

Fig. 9 Tafel plots for LBW UNS S32304 and SS304L immersed in 3.5% NaCl

$$IE\% = (i^{o}_{corros} - \frac{i_{corros}}{i^{o}_{corros}})x100 \tag{7}$$

where $IE\%$ denotes the percentage of the material that is exposed to corrosion, i^{o}_{corros} specifies the corrosion current density, and i_{corros} denotes corrosion length.

The anodic and cathodic Tafel lines for the LBW combination of UNS S32304 and SS304L in a 3.5% NaCl solution exhibit a parallel trend with increasing concentrations of the corrosion inhibitor. This behavior suggests that the inhibitors primarily function by block of the surfaces of the welded material. The inhibition efficiencies increase with higher concentrations of the inhibitors in the chloride mediums, as outlined in Table 3. The introduction of the inhibitors shifts the corrosion potential (E_{corr}) towards the positive side, indicating a mixed-type inhibitor with an anodic predominance in the 3.5% NaCl solution.

Adsorption consideration

The impedance data indicates that the organic inhibitor undergoes adsorption onto the surface of corroding metals, resembling a substitution process where the inhibitor displaces water molecules previously adsorbed on the metal surface. Among the temperatures investigated, the best correlation between experimental result and isotherm functions is observed when employing the Freundlich's adsorption isotherms. This particular adsorption isotherm is characterized by the following equation:

$$\log\ \theta = \log\ K_{rds} + n\ \log\ H \tag{8}$$

where H represents the inhibitor concentrations, θ denotes the degree of coverages on the metal surfaces, while K_{rds} and η represent the equilibrium constant for the adsorption–desorption processes. The selection of the most fitting isotherm is based on the correlation coefficient as indicated in Table 4. A plot of log θ versus log H resulted in a straight line in the chloride mediums, as depicted in Fig. 5. Notably, all linear correlations

Table 11 Effect of temperature

Temperature (K)	K_{rds}	ΔG_{rds}(kJ/mol)	n	R_2
307	6.6446	− 12.813	0.208	0.875
312	6.5436	− 15.767	0.214	0.872
317	5.7878	− 15.623	0.215	0.882
322	4.8883	− 14.863	0.366	0.872
327	5.8315	− 17.2936	0.429	0.873

coefficient equaled 1, and the value of n is consistent. These findings support Freundlich-type isotherms in the chloride medium, indicating physisorption of 1-BMIC. The calculated K_{rds} values from the intercepts on the $\theta - axis$ (Table 4) exhibit a decrease with rising temperature, implying that the inhibitor is physically adsorbed on the LBW UNS S32304 + SS304L surface in both media. The equilibriums constant of adsorptions, K_{rds}, is interconnected with the standard free energy of adsorptions, ΔG^o_{rds}, through the following equations:

$$\Delta G^o_{rds} = -RT \ln(55.5\, K_{rds}) \tag{9}$$

In the specified equation, R represents the gas constants, T specifies temperatures, and 55.5 corresponds to the molar concentrations of waters in the solutions. Examining Table 4, the negative ΔG^o_{rds} values affirm the spontaneity of the adsorption processes and the stability of the adsorbed layers on the steel surfaces. Typically, ΔG^o_{rds} value around − 20 kJ/mol or lowering is indicative of physisorption's, while around − 42 kJ/mol involve chemisorption. The values of ΔG^o_{rds} as presented in Table 4 suggest that the molecules undergo physisorption. The presence of heteroatoms in the inhibitor molecule facilitates its ready adsorption on the metal surface, forming an insoluble and stable film that mitigates metal dissolution.

Effect of temperatures

Corrosion reaction is commonly considered Arrhenius process, and the rates (ρ) are described by the following relationship:

$$\log\, \gamma = \log\, C - \frac{K_a}{2.303RT} \tag{10}$$

where γ represents the corrosion rate determined through weight loss measurements, K_a denotes the apparent activation energy, C represents Arrhenius constant, and R stands for the molar gas constant. The regression between log γ and $1/T$ is computed using a computer, and the resulting parameters are presented in Table 11. Arrhenius plots illustrating the correlation between log ρ *and* $\frac{1}{T}$ for both the blank and various concentrations of corrosion medium in the chloride medium are depicted in Fig. 10 and Fig. 11. The slope of the line corresponds to $\frac{-E_a}{2.303R}$, and the extrapolated intercept of the line at $(1/T = 0)$ yields log γ.

The observed higher values of activation energy (Ea) in the presence of the inhibitor, as indicated by the Arrhenius plots, suggest a significant inhibition of the corrosion reaction in LBW UNS S32304 + SS304L. In the Arrhenius plots, the activation energy is represented

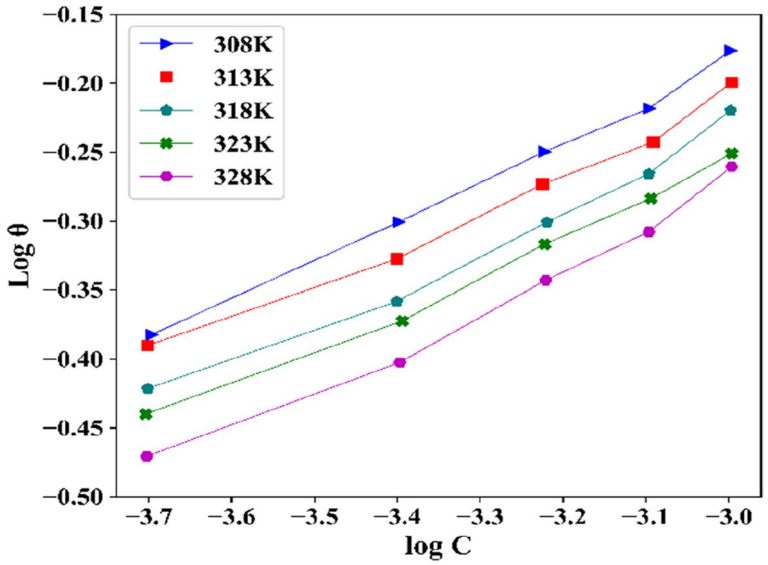

Fig. 10 Plot of log C versus log θ for LBW UNS S32304 and SS304L in 3.5% NaCl

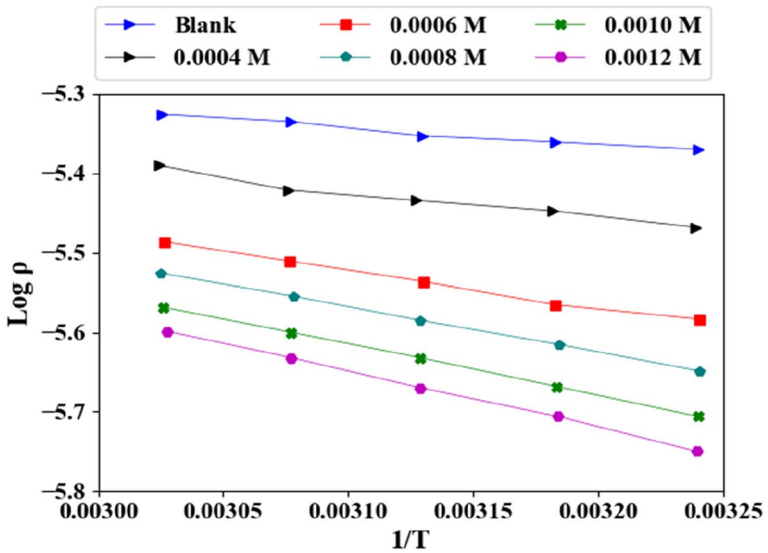

Fig. 11 Arrhenius plots for LBW UNS S32304 + SS304L in the absence and presence of varying concentration of NaCl

by the slope of the linear relationship between the natural logarithm of the corrosion rate and the reciprocal of the absolute temperature (1/T). When inhibitors are present, the activation energy increases, indicating a higher energy barrier for the corrosion reaction to proceed. This increase in activation energy is consistent with the manifestation of physical adsorption of the inhibitor molecules onto the metal surface, forming a protective barrier and impeding the corrosion process. Therefore, the correlation between the higher activation energy values in the presence of the inhibitor and the manifestation of physical adsorption support the conclusion that the inhibitor effectively inhibits the corrosion reaction in LBW UNS S32304 + SS304L.Conversely, the alteration of enthalpy (ΔH^o) and entropy

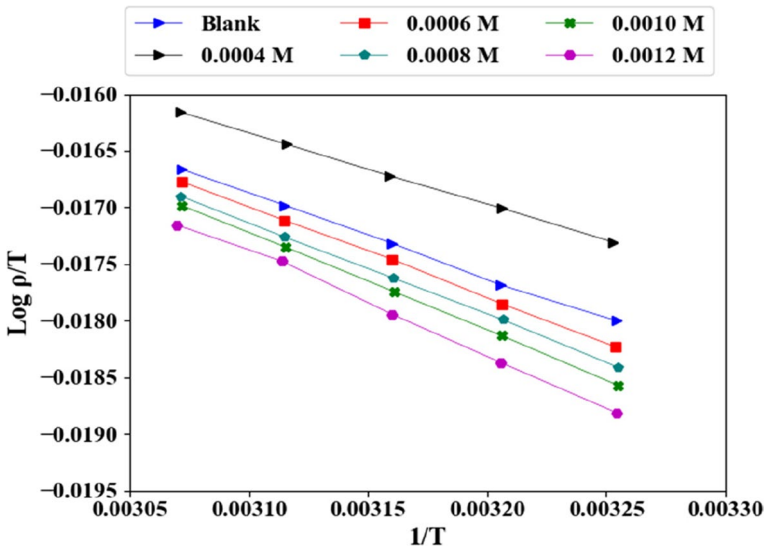

Fig. 12 Transition state plots for LBW UNS S32304 and SS304L

(ΔS^o) of activations for the formations of the activation complexes in the transition states is derived from the transition state equations:

$$\log \frac{\gamma}{T} = [(\log (\frac{R}{qN})) + (\frac{\Delta S^o}{2.303R})] - \frac{\Delta H^o}{2.303RT} \tag{11}$$

The equation provided involves the Planck constant (q) and Avogadro's number (N). A graph of $og \frac{\gamma}{T}$ vs. $^1/_T$ exhibits a linear relationship in chloride medium. The slope of the line corresponds to $\frac{-\Delta H^o}{2.303RT}$, while the intercept is $[(\log (R/qn) + (\Delta S^o/2.303 R)$. From these values, $\triangle H°$ and $\triangle S°$ are calculated. The inhibition efficiency values derived from the electrochemical impedance spectroscopy (EIS) align well with the result from weight losses and potentiodynamic polarizations measurement, as illustrated in Fig. 12.

Scanning electron microscopy

SEM images are captured to investigate the interactions between organic molecules and a metal surface. Fig. 13 depicts SEM images of a polished LBW UNS S32304+SS304L, with one image showing LBW UNS S32304+SS304L immersed in 3.5% NaCl for 24 h. The SEM analysis revealed notable differences between the specimens subjected to the inhibitor solutions and those immersed solely in 3.5% NaCl.

In the presence of the inhibitor, the LBW UNS S32304+SS304L surface appeared smoother, indicating better conditions compared to the rough and corrosion-covered surface observed in the absence of the inhibitor. Specifically, the inhibitor facilitated the formation of an organic film on the steel surface, thereby reducing the corrosion rate. Table 12 specifies the activation parameter of the dissolution's reactions of steel in 3.5% NaCl.

The specimen is LBW, featuring UNS S32304 on the left and SS304L on the right. Two heat-affected zones (HAZ), labeled as A and B, surround the weld region situated at the

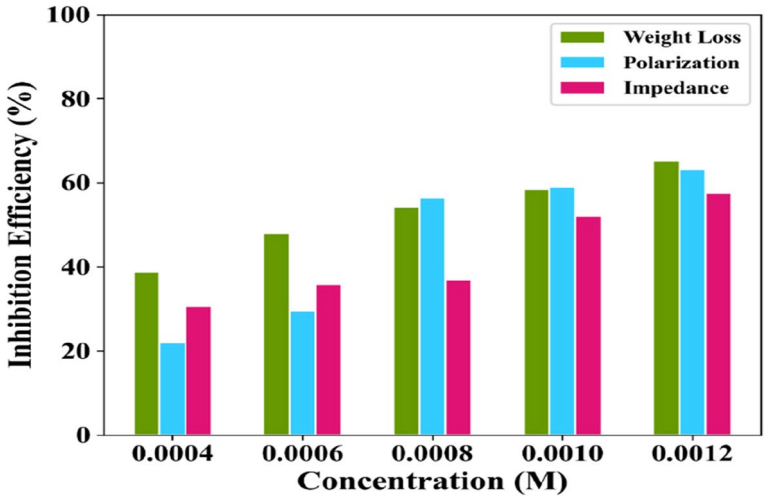

Fig. 13 Comparison of inhibition efficiencies value obtained by weight losses, polarizations, and impedance measurements of LBW UNS S32304 + SS304L in 3.5% NaCl

Table 12 Activation parameter of the dissolution's reactions of steels in 3.5% NaCl

Concentration (*M*)	$A\ (g\ cm^{-2}\ \min^{-1})$	$E_a(kJ/mol)$	$\Delta H.(kJ/mol)$	$\Delta S.(J/mol/K)$
-	3.718×10^{-5}	5.7831	0.1297	− 12.042
0.0004	2.346×10^{-4}	11.3454	0.1296	− 12.042
0.0006	4.606×10^{-4}	11.7823	0.1645	− 12.042
0.0008	4.817×10^{-4}	13.3265	0.1675	− 12.042
0.0010	7.254×10^{-4}	12.7335	0.1736	− 12.042
0.0012	3.729×10^{-3}	18.1194	0.1673	− 12.042

center. This configuration in Fig. 14 provides a concise overview of the materials and zones involved in the laser welding process.

Observations of the SEM evaluation

Following are the observations of the SEM evaluations made from Fig. 15a, b, c, d, and e.

➢ HAZ (A)

- *Microstructure*: Minimal grain growth and fine precipitates uniformly distributed
- *Corrosion properties*: The minimal grain growth suggests optimal heat input during welding, leading to a stable microstructure. Fine precipitates enhance corrosion resistance by providing additional barriers to corrosion. The absence of microcracks or pitting indicates high integrity, further supporting good corrosion performance.

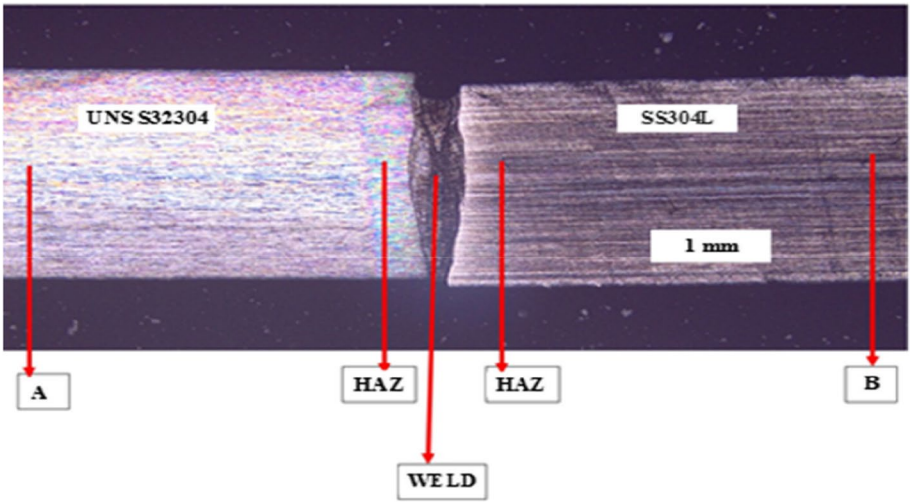

Fig. 14 LBW UNS S32304 + SS304L for SEM observation

➢ HAZ (B)

- *Microstructure*: Some grain growth and slightly clumped precipitates in certain areas
- *Corrosion properties*: While grain growth remains within acceptable limits, the clumping of precipitates may indicate potential areas of localized corrosion. Further investigation is warranted to assess the impact of precipitate clustering on corrosion resistance. Overall, the stable microstructure suggests good corrosion performance, but potential localized corrosion sites should be monitored.

➢ Ø Location (A) (base metal — SS304L)

- *Microstructure*: Minimal surface degradation and no significant intergranular or pitting corrosion
- *Corrosion properties*: The refined microstructure and minimal intergranular corrosion suggest excellent corrosion resistance. Isolated shallow pitting indicates localized corrosion, but overall, the material demonstrates high stability and long-term durability in the saline environment.

➢ Ø Location (B) (base metal — UNS S32304)

- *Microstructure*: Minimal surface degradation and no significant intergranular or pitting corrosion
- *Corrosion properties*: The refined microstructure and minimal intergranular corrosion suggest excellent corrosion resistance. Isolated shallow pitting indicates localized corrosion, but overall, the material demonstrates high stability and long-term durability in the saline environment.

➢ Ø Weld

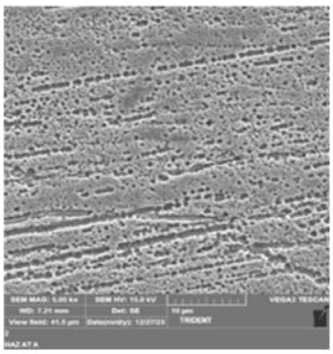

Uniform grain distribution with minimal surface defects observed in UNS S32304 base metal

(a) HAZ at A

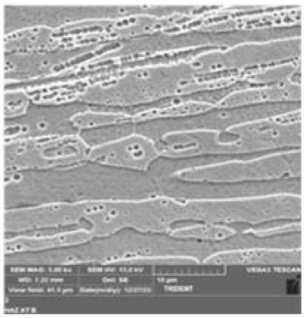

Fine-grained microstructure with limited surface irregularities detected in SS304L base metal

(b) HAZ at B

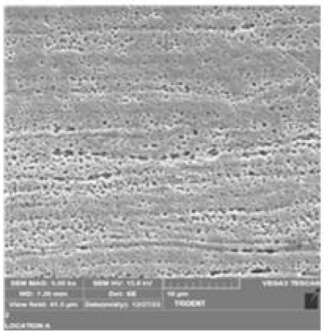

Well-defined weld interface exhibiting intermetallic phases and possible fusion defects

(c) Region of Location 'A'

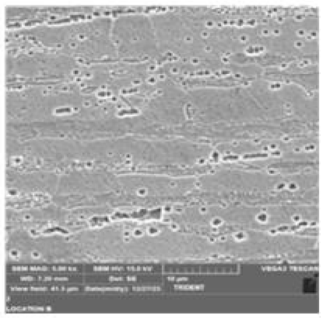

Corrosion pits and surface irregularities evident on the welded specimen, indicating localized degradation.

(d) Region of Location 'B'

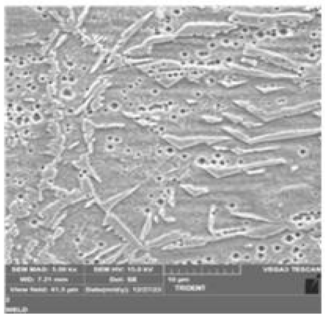

Distinct grain boundaries and weld pool solidification features observed in the laser beam welded joint

(e) Weld Location

Fig. 15 **a** HAZ at A (**b**). HAZ at B (**c**). Region of location "A" (**d**). Region of location "B". **e** Weld location

- *Microstructure*: Fine, equiaxed grain structure, and finely dispersed precipitates
- *Corrosion properties*: The fine grain structure minimizes potential corrosion initiation sites, while finely dispersed precipitates promote uniform passivation, enhancing overall resistance. The excellent cohesion at the weld-HAZ interface eliminates a potential weak point, contributing to the material's robust corrosion performance.

Table 13 XRD analysis results for SS304L + UNS S32304 laser beam welded sample

Compound/phase	XRD peaks (2θ)	Alpha values
Austenite (γ-Fe)	44.72, 64.28	0.9–1.0
Ferrite (α-Fe)	42.53, 50.68	0.1–0.5
Sigma phase (σ)	47.82, 67.93	Varies
Chromium carbides (Cr_3C_2)	35.53, 81.03	Varies

The correlation behavior becomes apparent when analyzing various sections of the welded specimen. The specific microstructural features observed, such as grain size, precipitate distribution, and interfacial bonding, directly influence the material's corrosion resistance by affecting factors such as surface passivation and susceptibility to localized corrosion.

EDX analysis

Table 1 represents the X-ray diffraction (XRD) analysis results conducted on a laser beam welded sample composed of SS304L (stainless steel 304L) alloy combined with UNS S32304, a duplex stainless-steel alloy. XRD analysis is a robust method utilized for identifying the crystalline phases present in a material. It achieves this by examining the diffraction patterns generated when X-rays interact with the atomic arrangement of the material. In this study, the aim is to characterize the phases formed in the welded region of the SS304L+UNS S32304 sample, which is crucial for assessing its structural integrity and performance. The compounds or phases identified in the XRD analysis are presented in Table 1. The first phase identified is austenite (γ-Fe), which is the predominant phase in stainless steel alloys like SS304L and contributes to their corrosion resistance and strength. The characteristic XRD peaks for austenite appear at 2θ values of 44.72 and 64.28°. The alpha values associated with austenite range from 0.9 to 1.0, indicating a high proportion of this phase in the welded sample. The second phase identified is ferrite (α-Fe), which is another common phase in stainless steel alloys, and contributes to their toughness and ductility. Table 13 shows the XRD analysis results for SS304L+UNS S32304 laser beam welded sample.

Ferrite peaks are observed at 2θ values of 42.53 and 50.68° in the XRD pattern. The corresponding alpha values for ferrite range from 0.1 to 0.5, suggesting a moderate presence of this phase in the welded sample. Additionally, the XRD analysis detected the presence of sigma phase (σ) and chromium carbides (Cr_3C_2) in the sample. Fig. 16 shows the XRD analysis of the LBW SS304L+UNS S32304.

Sigma phase is a deleterious intermetallic phase that detrimentally affects the mechanical properties and corrosion resistance of stainless-steel alloys. The characteristic XRD peaks for Sigma phase are observed at 2θ values of 47.82 and 67.93°. The alpha values for sigma phase vary, indicating its variable presence in different regions of the sample. Chromium carbides, represented by peaks at 2θ values of 35.53 and 81.03°, are carbide precipitates form during welding processes and may affect the material's corrosion resistance. The presence of chromium carbides is indicated by varying alpha values, the XRD analysis revealed the presence of multiple phases in the laser beam welded SS304L+UNS S32304 sample, including austenite, ferrite, sigma

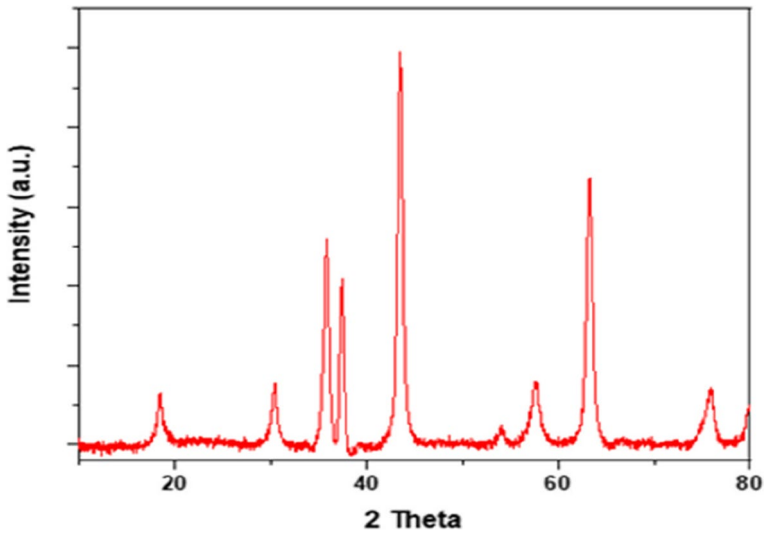

Fig. 16 XRD analysis of the LBW SS304L + UNS S32304

phase, and chromium carbides. The composition and distribution of these phases play a critical role in determining the material's mechanical properties, corrosion resistance, and overall performance. These findings provide valuable insights for optimizing the welding process parameters and enhancing the quality and reliability of welded stainless-steel components.

Conclusion

➢ Increased solution temperature (up to 50 °C) resulted in a slight decrease in corrosion resistance for both UNS S32304 and SS304L base metals. However, the LBW maintained superior performance even at elevated temperatures, exhibiting only a 5% reduction in breakdown potential compared to a 10% decrease for the base metals at 50 °C.

➢ SEM analysis revealed minimal surface adsorption of Cl^- ions on both base metals and the weld metal after exposure. This indicates effective passivation by chromium oxide layers, preventing significant chloride ingress and subsequent pitting initiation.

➢ Quantitative analysis showed an average Cl^- ion coverage of 0.25% on the weld metal compared to 0.5% on the base metals, further highlighting the superior adsorption resistance of the weld.

➢ Tafel plots demonstrated a significant shift in corrosion potential for the weld metal compared to the base metals, indicating a higher nobility and enhanced corrosion resistance.

➢ The weld metal exhibited a corrosion current density of 0.5 $\mu A/cm^2$ compared to 1.2 $\mu A/cm^2$ for UNS S32304 and 2.0 $\mu A/cm^2$ for SS304L, signifying a 60% and 75% reduction in corrosion rate, respectively.

➢ These findings confirm the effectiveness of the LBW process in promoting corrosion resistance and improving the overall material stability.

➢ EIS analysis revealed a higher Nyquist semicircle diameter for the weld metal compared to the base metals, indicating higher impedance and stronger passive film formation.

➢ The charge transfer resistance values are 25 $k\Omega.cm^2$ for the weld metal, 15 $k\Omega \cdot cm^2$ for UNS S32304, and 10 $k\Omega.cm^2$ for SS304L, demonstrating a 67% and 150% improvement in barrier properties for the weld over the base metals. This confirms the enhanced protective ability of the weld metal and its effectiveness in mitigating corrosion attack.

➢ The promising solution holds potential for applications requiring elevated corrosion resistance in chloride-rich environments, laying the foundation for future research on long-term durability, welding parameters, corrosion inhibitors, and advanced treatments.

➢ Notably, the welded metal exhibited superior corrosion resistance compared to the base metal. This enhancement is attributed to the utilization of LBW renowned for its precision and minimal heat-affected zones. By carefully controlling welding parameters and implementing post-weld treatments, efforts are made to mitigate differences between the base and welded metals. These factors likely contributed to the observed higher corrosion resistance in the welded metal.

While our current study focused on the corrosion behavior of the laser beam-welded combination of UNS S32304 and SS304L without post-heat treatment, there is potential for further investigation into the effects of heat treatment on the weld joint. Subsequent studies could explore the impact of post-heat treatment on the corrosion resistance and mechanical properties of the weld, providing valuable insights into optimizing the welding process for enhanced performance in corrosive environments. Additionally, examining the microstructural changes induced by heat treatment and their influence on the overall stability of the weld would be of great interest to researchers and industry professionals alike. Incorporating post-heat treatment into future research endeavors will contribute to a comprehensive understanding of the welding process and facilitate the development of strategies for achieving even greater corrosion resistance and material stability in practical applications.

Abbreviations

LBW	Laser beam welding
UNS	Unified Numbering System
DSS	Duplex stainless steels
CPT	Critical pitting temperatures
GMAW	Gas metal arc welding
EBW	Electron beam welding
LPBF	Laser powder bed fusion
SCC	Stress corrosion cracking
HA	Hydroxyapatite
EIS	Electrochemical impedance spectroscopy
SEM	Scanning electron microscopy
WL	Weight losses
IE	Inhibitions efficiencies
HCl	Hydrochloric acid
AC	Alternating current
HAZ	Heat-affected zones
XRD	X-ray diffraction

Acknowledgements
None

Authors' contributions
All the authors have contributed equally to the work.

Funding
This research did not receive any specific grant from funding agencies in the public, commercial, or not-for-profit sectors.

Availability of data and materials
Data sharing is not applicable to this article as no datasets were generated or analyzed during the current study.

Declarations

Ethics approval and consent to participate
All applicable institutional and/or national guidelines for the care and use of animals were followed.
For this type of analysis, formal consent is not needed.

Competing interests
The authors declare that they have no competing interests.

Received: 26 February 2024 Accepted: 15 June 2024
Published online: 09 July 2024

References

1. Al-Moubaraki AH, Obot IB (2021) Corrosion challenges in petroleum refinery operations: sources, mechanisms, mitigation, and future outlook. J Saudi Chem Soc 25:101370
2. Groysman A (2017) Corrosion problems and solutions in oil, gas, refining and petrochemical industry. Koroze a ochr mater 61:100–117
3. Alamri AH (2020) Localized corrosion and mitigation approach of steel materials used in oil and gas pipelines – an overview. Eng Fail Anal 116:104735
4. Ogunsanya IG, Hansson CM (2020) Reproducibility of the corrosion resistance of UNS S32205 and UNS s32304 stainless steel reinforcing bars. Corrosion 76:114–130
5. Lacerda JC, Teixeira RL, Souza RM, Soares RB, Lins V de (2020) Pitting corrosion behavior of UNS S31803 and UNS S32304 duplex stainless steels in 3.5 wt% NaCl solution. Matéria (Rio de Janeiro). https://doi.org/10.1590/s1517-707620200002.1022
6. Ferreira dos Santos N, Esteves L, Nery Garcia JH, Júnior RC, Modenesi PJ, Pereira da Silva B, Aoki IV, da Costa R, Campos W (2020) Microstructural and corrosion resistance of lean duplex stainless steel UNS S32304 welded by saw with cold wire addition. Corros 76:619–627
7. Qi L, Gui S-J, Tang P, Wang X-H (2021) Corrosion resistance of two types of stainless steel reinforcements under the simulated seawater wetting-drying cycle attack. IOP Conference Series: Earth and Environmental Science 643:012100
8. Martin U, Bastidas DM (2023) Integrity assessment of stress corrosion cracking susceptibility of duplex UNS S32205 and austenitic UNS S31653 stainless steel reinforcements. Metals 13:1932
9. Buddu RK, Chauhan N, Raole PM, Natu H (2015) Studies on mechanical properties, microstructure and fracture morphology details of laser beam welded thick SS304L plates for fusion reactor applications. Fusion Eng Design 95:34–43
10. Mosavi A, Soleimani A, Karimi A, Akbari M, Karimipour A, Karimipour A (2020) Investigating the effect of process parameters on the mechanical properties and temperature distribution in fiber laser welding of AISI304 and AISI 420 sheet using response surface methodology. Infrared Phys Technol 111:103478
11. Öhlin O, Gullberg D (2022) Corrosion properties of UNS S83071, super duplex stainless steel with high acid corrosion resistance. AMPP CORROSION D041S042R008
12. Zhang Y, Cheng S, Wu S, Cheng F (2020) The evolution of microstructure and intergranular corrosion resistance of duplex stainless steel joint in multi-pass welding. J Mater Process Technol 277:116471
13. Zhang D, Wen P, Yin B, Liu A (2021) Temperature evolution, phase ratio and corrosion resistance of duplex stainless steels treated by laser surface heat treatment. J Manuf Process 62:99–107
14. Silva D, Lima L, Araújo A, Silva V, Raimundo R, Damasceno I, Simões T, Gomes R (2020) The effect of microstructural changes on mechanical and electrochemical corrosion properties of duplex stainless steel aged for short periods. Mater 13:5511
15. Heider B, Oechsner M, Reisgen U, Ellermeier J, Engler T, Andersohn G, Sharma R, Gonzalez Olivares E, Zokoll E (2020) Corrosion resistance and microstructure of welded duplex stainless steel surface layers on gray cast iron. J Therm Spray Technol 29:825–842
16. Zhang S, Feng H, Li H, Jiang Z, Zhang T, Zhu H, Lin Y, Zhang W, Li G (2023) Design for improving corrosion resistance of duplex stainless steels by wrapping inclusions with niobium armour. Nature Commun. https://doi.org/10.1038/s41467-023-43752-8
17. Kawamori M, Kinugasa J, Katsuki Y, Nishizawa N, Nagao M (2023) Mechanism of improving corrosion resistance in heat affected zone of duplex stainless steel by tantalum addition. Corros Sci 227:111748
18. Ma Q, Luo C, Liu S, Li H, Wang P, Liu D, Lei Y (2021) Investigation of arc stability, microstructure evolution and corrosion resistance in underwater wet FCAW of duplex stainless steel. J Mater Res Technol 15:5482–5495

19. Liu Z, Xie Y, Chu X, Zhang L, Zhao W, Zhao C, He H (2023) Evolution of the sigma phase and its effect on the corrosion resistance of ASTM A890 3A duplex stainless steel. Mater Today Commun 36:106926
20. Zhang Y, Cheng F, Wu S (2021) Improvement of pitting corrosion resistance of wire arc additive manufactured duplex stainless steel through post-manufacturing heat-treatment. Mater Charact 171:110743
21. Chen Y, Yang B, Zhou Y, Wu Y, Zhu H (2020) Evaluation of pitting corrosion in duplex stainless steel fe20cr9ni for nuclear power application. Acta Mater 197:172–183
22. Miranda-Pérez A, Rodríguez-Vargas B, Calliari I, Pezzato L (2023) Corrosion resistance of GMAW duplex stainless steels welds. Mater 16:1847
23. Torres C, Johnsen R, Iannuzzi M (2021) Crevice corrosion of solution annealed 25Cr duplex stainless steels: effect of W on critical temperatures. Corros Sci 178:109053
24. Singh J, Shahi AS (2020) Metallurgical and corrosion characterization of electron beam welded duplex stainless steel joints. J Manuf Process 50:581–595
25. Fedorov A, Zhitenev A, Strekalovskaya D (2021) Effect of heat treatment on the microstructure and corrosion properties of cast duplex stainless steels. E3S Web of Conferences 225:01003
26. Köhler ML, Kunz J, Herzog S, Kaletsch A, Broeckmann C (2021) Microstructure analysis of novel LPBF-processed duplex stainless steels correlated to their mechanical and corrosion properties. Mater Sci Eng: A 801:140432
27. Xiao Y, Tang J, Wang Y, Lin B, Nie Z, Li Y, Normand B, Wang H (2022) Corrosion behavior of 2205 duplex stainless steel in NaCl solutions containing sulfide ions. Corros Sci 200:110240
28. Silva DDS, Simões TA, Macedo DA, Bueno AHS, Torres SM, Gomes RM (2021) Microstructural influence of sigma phase on pitting corrosion behavior of duplex stainless steel/NaCl electrolyte couple. Mater Chem Phy 259:124056
29. Oh S, Kim D, Kim K, Kim D-I, Chung W, Shin B-H (2023) The effect of surface roughness on re-passivation and pitting corrosion of super duplex stainless steel UNS S 32760. Int J Electrochem Sci 18:100351
30. Rajaguru J, Arunachalam N (2021) Effect of machined surface integrity on the stress corrosion cracking behaviour of super duplex stainless steel. Eng Fail Anal 125:105411
31. Raj PN, Navaneethkrishnan PK, Sekar K, Joseph MA (2020) Comparative study of mechanical, corrosion and erosion—corrosion properties of cast hyper-duplex and super-duplex stainless steels. Int J Minerals, Metallurgy Mater 27:954–961
32. Köse C (2020) Characterization of weld seam surface and corrosion behavior of laser-beam-welded AISI 2205 duplex stainless steel in simulated body fluid. J Mater Sci 55(36):17232–17254
33. Köse C (2022) Heat treatment and heat input effects on the dissimilar laser beam welded AISI 904L super austenitic stainless steel to AISI 317L austenitic stainless steel: surface, texture, microstructure and mechanical properties. Vacuum 205:111440
34. Köse C, Topal C (2023) Dissimilar laser beam welding of AISI 2507 super duplex stainless to AISI 317L austenitic stainless steel. Mater Sci Eng A 862:144476
35. Köse C (2023) Fiber laser beam welding of additive manufactured 316L austenitic stainless steel with wrought 2507 super duplex and wrought 904L super austenitic stainless steels: crystallographic texture, microstructure, and mechanical properties. Vacuum 215:112347
36. Ceyhun KÖSE, Kacar R, ZORBA AP, BAĞIROVA M, ABAMOR EŞ, Allahverdiyev AM (2018) Interactions between fibroblast cells and laser beam welded AISI 2205 duplex stainless steel. Mater Sci 24(2):159–165

Publisher's Note